Physics of Fluids

Modeling the interplay between the shear layer and leading edge suction during dynamic stall

Cite as: Phys. Fluids **31**, 107104 (2019); https://doi.org/10.1063/1.5121312
Submitted: 24 July 2019 . Accepted: 13 September 2019 . Published Online: 03 October 2019

Julien Deparday, and Karen Mulleners

Physics of Fluids ARTICLE scitation.org/journal/phf

Modeling the interplay between the shear layer and leading edge suction during dynamic stall

Cite as: Phys. Fluids 31, 107104 (2019); doi: 10.1063/1.5121312
Submitted: 24 July 2019 • Accepted: 13 September 2019 •
Published Online: 3 October 2019

Julien Deparday and Karen Mulleners[a]

AFFILIATIONS

UNFoLD, Institute of Mechanical Engineering, École Polytechnique Fédérale de Lausanne (EPFL), CH-1015 Lausanne, Switzerland

[a]Electronic mail: karen.mulleners@epfl.ch

ABSTRACT

The dynamic stall development on a pitching airfoil at $Re = 10^6$ was investigated by time-resolved surface pressure and velocity field measurements. Two stages were identified in the dynamic stall development based on the shear layer evolution. In the first stage, the flow detaches from the trailing edge and the separation point moves gradually upstream. The second stage is characterized by the roll up of the shear layer into a large scale dynamic stall vortex. The two-stage dynamic stall development was independently confirmed by global velocity field and local surface pressure measurements around the leading edge. The leading edge pressure signals were combined into a single leading edge suction parameter. We developed an improved model of the leading edge suction parameter based on thin airfoil theory that links the evolution of the leading edge suction and the shear layer growth during stall development. The shear layer development leads to a change in the effective camber and the effective angle of attack. By taking into account this twofold influence, the model accurately predicts the value and timing of the maximum leading edge suction on a pitching airfoil. The evolution of the experimentally obtained leading edge suction was further analyzed for various sinusoidal motions revealing an increase in the critical value of the leading edge suction parameter with increasing pitch unsteadiness. The characteristic dynamic stall delay decreases with increasing unsteadiness, and the dynamic stall onset is best assessed by critical values of the circulation and the shear layer height which are motion independent.

I. INTRODUCTION

The sudden stall from a dynamically pitching airfoil is a classic example of unsteady flow separation with applications in rotary aircraft, rapidly maneuvering fixed wing aircraft, and wind turbines. The unsteady change in angle of attack leads to a delay in stall onset and an increase in the maximum attainable lift with respect to the static response. Although stall delay and lift overshoot sound beneficial, dynamic stall is generally a phenomenon that is to be avoided. Large excursions of the highly unsteady aerodynamic loads following stall onset decrease the aerodynamic efficiency and yield strong vibrations and increasing structural forces and bending moments that cause fatigue and potential damage to the airfoil and the structure supporting it.[1–3]

Early research on dynamic stall was focused on understanding the main evolution and succession of flow phenomena and the effect of the kinematic parameter on the aerodynamic forces and pitching moment of the airfoil.[4–8] Smoke flow visualization was used to qualitatively describe the coherent vortex structures developing during dynamic stall. The development of unsteady pressure sensors made it possible to obtain accurate spatially and temporally resolved surface pressure distributions and measure high frequency turbulent flow oscillations.[9–13] The surface pressure measurements revealed the presence and continued growth of a suction peak at the leading edge during dynamic stall development. The use of time-resolved particle image velocimetry (PIV) allowed for accurate flow field measurements that were analyzed to reveal the dominant role of the dynamic stall vortex and its characteristic time

scales.[14–18] Recent high-fidelity large eddy simulations[19,20] as well as direct numerical simulations[21] of dynamic stall on a pitching airfoil show excellent agreement with experimental results.[22] Numerical simulations provide the complete flow field information, including velocity field, airfoil surface pressure, and surface friction data, but they remain computationally expensive for Reynolds numbers above 5×10^5.

To protect the integrity of the airfoil and the supporting structure and avoid loss of aerodynamic performance, it is essential to accurately predict the dynamic stall development and onset. The response of the flow to unsteady changes in angle of attack is nonlinear and depends on many parameters such as the airfoil profile, inflow Reynolds number, and motion kinematics. If the angle of attack is increased fast enough to an angle above the static stall limit, flow will separate from the leading edge.[23–29] It thus seems natural to search for the indication of massive dynamic flow separation near the leading edge. As early as 1959, Evans and Mort[30] presented evidence of a correlation between the minimum value of the leading edge surface pressure coefficient and the steepness of the adverse pressure gradient at stall. Leishman and Beddoes[31] defined their stall onset criterion for incompressible flows based on the work of Evans and Mort.[30] They related the critical leading edge pressure to a critical normal force coefficient to derive a practical stall onset criterion for their dynamic stall model that predicts the aerodynamic loads for unsteady angle of attack variations. The influence of the unsteady conditions that were taken into account is twofold. Due to the unsteady change in angle of attack, there is a lag in the increase in the normal force coefficient with angle of attack and there is a lag in the leading edge pressure response with respect to the normal force coefficient. As a consequence, the critical leading edge pressure will be reached at a higher value of the normal force coefficient, which in turn will be reached at a higher angle of attack with increasing pitch rate. Both effects are included in a deficiency function that describes the first order lag of the normal force coefficient with an empirical time constant that depends solely on the Mach number. The influence of progressive trailing edge separation, which is present in many dynamic stall cases even if they are dominated by leading edge separation, is represented in the Beddoes-Leishman model as a variation of the slope of the normal force coefficient curve in function of the angle of attack. The correction is based on Kirchhoff's law and includes an empirical evolution of the trailing edge separation location with angle of attack.[32]

Noteworthy improvements of the Beddoes-Leishman model include the works of Niven and Galbraith[33] and Sheng *et al.*[34] Niven and Galbraith[33] introduced an additional empirical time constant adding to the lag of the normal force coefficient representing the finite time required for the disturbed flow to develop into a vortex. They also presented an extension of the Kirchhoff law in the unsteady regime to improve the predictions of the dynamic stall model for scenarios where trailing edge flow reversal is nonnegligible. According to Niven and Galbraith,[33] a more esthetic prediction of dynamic stall onset should be based on a quantifiable feature of the unsteady trailing edge flow reversal behavior. Sheng *et al.*[34] criticized the uncertainties associated with the upper and lower bounds of the critical leading edge pressure from the Evans and Mort correlation[30] and proposed a new criterion for stall onset that is based on a critical angle of attack instead of a critical normal force coefficient. This new criterion relies on a linear variation of the dynamic stall onset angle of attack with pitch-rate for ramp-up motions which does not hold for lower pitch rates and in scenarios where unsteady trailing edge flow reversal is observed.

A more recent stall onset criterion that has rapidly gained popularity is the critical leading edge suction parameter criterion proposed by Ramesh *et al.*[35] This criterion was initially developed for application in discrete vortex models.[36,37] It is based on the idea that an airfoil can support a maximum amount of leading edge suction. If this maximum limit is exceeded, vorticity is released from the leading edge, accumulates, and forms a leading edge or dynamic stall vortex. The critical value of the leading edge suction parameter depends on the airfoil shape and Reynolds number and is independent of the motion kinematics for scenarios where no trailing-edge separation is present.[38]

The leading edge suction parameter proposed by Ramesh *et al.*[35] is related to the first term of the Fourier series of the distribution of the vortex sheet strength along the camber line in thin airfoil theory. Thin airfoil theory determines the aerodynamic force on an airfoil as the result of the potential pressure field induced by a vortex sheet with strength distribution $\gamma(\theta, t)$ along the airfoil's camber line.[39] The vortex sheet strength distribution represents the deviation of the flow due to the presence of the airfoil, and it is calculated such that there is no net normal induced velocity along the camber line. The circulation distribution for a generalized camber line can be described as a Fourier series,

$$\gamma(\theta, t) = 2U_\infty \left(A_0(t) \frac{1 + \cos\theta}{\sin\theta} + \sum_{n=1}^{\infty} A_n(t) \sin n\theta \right), \tag{1}$$

where the angle θ is related to the chord wise coordinate x along the camber line through

$$x = \frac{c}{2}(1 - \cos\theta). \tag{2}$$

The time-dependent Fourier coefficients $A_n(t)$ are determined to satisfy the Kutta condition at the trailing edge (Fig. 1). The first Fourier coefficient A_0 represents the leading edge suction peak resulting from the acceleration of the flow around the airfoil's leading edge.[40]

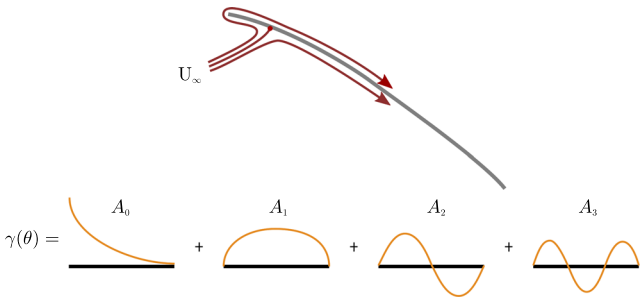

FIG. 1. Schematic representation of the flow around the leading edge of a thin airfoil and the associated vortex strength distribution γ of the vortex sheet representing the airfoil's camber line broken into the first 4 terms of the Fourier series (inspired by Katz and Plotkin[39]).

The critical values of the dynamic stall onset parameters summarized above are generally well defined for dynamic stall scenarios where trailing edge flow reversal is absent or suppressed. However, in most occurrences of dynamic stall, progressive trailing edge separation and flow reversal play a significant role.[12,19,20,41] In this paper, we consider experimental data of deep dynamic stall on a pitching airfoil where stall onset is the result of the roll-up of a free shear layer at the interface between the outer flow and a region of flow reversal near the airfoil's suction surface. We will analyze the interplay between the unsteady development of the free shear layer and the leading edge suction during dynamic stall development based on the experimental time-resolved velocity field and surface pressure data. Based on the results, we will propose a theoretical model of the leading edge suction parameter with the temporal evolution of the shear layer height as the quantifiable feature of the unsteady trailing edge flow reversal. The characteristic time scales of the evolution of the shear layer and the leading edge suction will be identified and compared, and critical values with regard to dynamic stall onset will be identified.

II. EXPERIMENTAL SETUP

The experimental data used for the current analysis stems from experiments that were conducted in a closed-circuit, low-speed wind tunnel of the German Aerospace Centre [Deutsches Zentrum für Luft- und Raumfahrt (DLR)] in Göttingen. The data from this measurement campaign were previously used to study the onset and development of dynamic stall.[14,43,44] The wind tunnel had an open test section with a rectangular nozzle of 0.75 × 1.05 m. Simultaneous unsteady surface pressure and time-resolved velocity field measurements using particle image velocimetry (PIV) were conducted for a sinusoidally pitching airfoil. The airfoil had an OA209 cross section profile, a chord length of $c = 0.3$ m, and an aspect ratio of 5. The airfoil was pitching around its quarter chord axis. The OA209 airfoil profile is a typical helicopter blade profile, and it represents a class of airfoils that are potentially affected by dynamic stall in reality. It was placed in a uniform flow of $U_\infty = 50$ m s^{-1} ($Re_c = 9.2 \times 10^5$). Measurements were taken in the cross-sectional plane at the model midspan.

The unsteady surface pressure distribution was determined using 41 surface-mounted pressure transducers, which were sampled at a rate of 6 kHz and integrated to obtain the lift history. The pressure data from the 13 pressure taps in the first 10% of the chord were integrated to obtain the leading edge suction S_{LE} vector (Fig. 2).

The velocity field was measured using stereo PIV with an acquisition rate of 1500 Hz. The PIV system consisted of a diode-pumped Nd:YAG laser (Lee Laser, LDP-200MQG Dual) that emitted laser pulses with an energy of approximately 12 mJ per pulse and two high speed CMOS cameras (Photron Ultima APX-RS) with 1024 × 1024 px sensors. The vertical plane at the model midspan was illuminated by the laser from above, and the cameras were mounted downstream of the airfoil in a stereoscopic setup alongside the wind tunnel's diffuser. The width of the field of view covered the entire chord for the relevant angle of attack range. Due to experimental limitations, valid velocity information was only available down to approximately 3 mm or 0.01c above the airfoil's surface. The time-resolved PIV data were evaluated using a multigrid algorithm with a final interrogation window size of 32 × 32 px and an overlap of approximately 80%, yielding a spatial resolution of 1.2 mm or 0.004c. The detection probability of a valid displacement in the PIV data was higher than 90%. The remaining spurious vectors were detected and replaced using the automated postprocessing algorithm of Garcia.[45] The relative measurement error was estimated to be less than 0.02 every where. More details about the PIV error estimation can be found in the work of Mulleners and Raffel.[43] The velocity fields were rotated into the airfoil frame of reference prior to analysis, with the x-axis along chord, the y-axis along span, and the z-axis upward perpendicular to the chord.

The angle of attack of the airfoil was varied sinusoidally around a mean incidence α_0, close to the static stall angle, with an amplitude α_1, and an oscillation frequency f_{osc}. A large range of dynamic stall cycles was obtained by varying these three motion parameters. The reduced frequencies $k = \pi f_{osc} c/U_\infty$ of all cases are between 0.05 and 0.1. The instantaneous effective unsteadiness $\dot{\alpha}^\star_{ss}$ was introduced previously by Mulleners and Raffel[14] as a single representative parameter to describe the influence of the motion parameters describing a sinusoidal pitching motion on dynamic stall development. It is defined as the rate of change in the angle of attack at the moment when the static stall angle is exceeded, and it is nondimensionalized by the convective time: $\dot{\alpha}^\star_{ss} = \dot{\alpha}_{ss} c/U_0$.

III. DYNAMIC STALL LIFE CYCLE

The typical dynamic stall flow development within a single pitching cycle is represented in Fig. 3 by means of selected instantaneous velocity fields. The color map represents the out-of-plane vorticity component $\omega_y = \partial u/\partial z - \partial w/\partial x$. The angle of attack in this example varies sinusoidally around a mean angle of attack of $\alpha_0 = 20°$ with an amplitude of $\alpha_1 = 8°$ and a reduced pitching frequency $k = 0.05$. We consider the start of the pitching cycle when the angle of attack is lowest. The first half of the cycle is referred

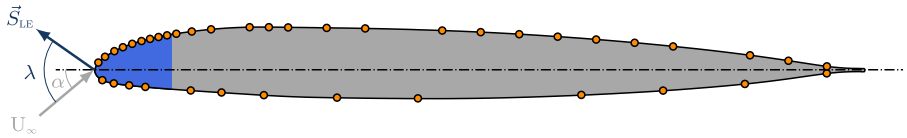

FIG. 2. Positions of pressure sensors on the airfoil shown by orange dots. The blue shaded region defines the leading edge section that is considered to calculate the leading edge suction vector S_{LE} and its chord wise component F_S that is used to calculate the experimental leading edge suction parameter. [Reprinted with permission from Deparday and Mulleners, J. Phys.: Conf. Ser. **1037**, 022017 (2018). Copyright 2018 IOP Publishing.]

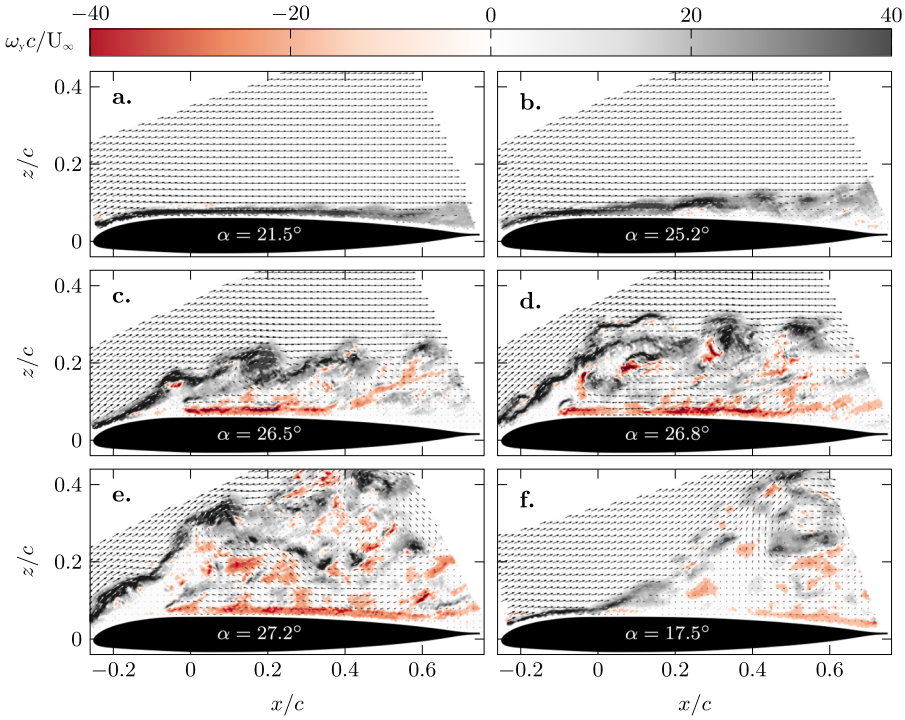

FIG. 3. Selected instantaneous velocity and vorticity field snapshots during a single sinusoidal pitching cycle described by α_0 = 20°, α_1 = 8°, k = 0.05, and normalized effective unsteadiness $\dot{\alpha}^*_{ss}$ = 0.013. The snapshots were taken at t/T = 0.28 (a), 0.36 (b), 0.40 (c), 0.41 (d), 0.43 (e), 0.80 (f) within the same pitching cycle. The timing of the snapshots is also indicated in the lift history in Fig. 4. [Reproduced with permission from Deparday and Mulleners, J. Phys.: Conf. Ser. **1037**, 022017 (2018). Copyright 2018 IOP Publishing.]

to as the pitch-up motion, and the second half is referred to as the pitch-down motion. The maximum angle of attack in the presented case is α_{max} = 28° and well beyond the static stall angle of attack α_{ss} = 21.4° under the given circumstances. The temporal history of the lift coefficient during the dynamic stall cycle is presented in Fig. 4 and displays the characteristic features of deep dynamic stall including stall delay to an angle of attack beyond the static stall angle, lift overshoot with respect to the maximum static lift, and large load fluctuations following dynamic stall. The timing of the individual snapshots in Fig. 3 is indicated in the lift history. The evolution of the circulation during the selected pitching cycle is also included in Fig. 4. The solid line represents the positive circulation calculated by integrating all positive vorticity in the field of view, and the dashed line represents the negative circulation calculated by integrating all negative vorticity in the field of view. The leading edge vortex has positive signed circulation, and the trailing edge vortex has negative circulation. The evolution of the shear layer is characterized in terms of its dimensionless average shear layer height Δz^* [Fig. 4(c)]. It is defined as the dimensionless chord wise averaged chord-normal distance between the shear layer location and the airfoil's suction surface at any given time.[43] The shear layer location is identified in individual velocity field snapshots by the location of clock wise rotating shear layer vortices that in turn are identified using Eulerian vortex criteria.[14,46]

The temporal evolution of the dynamic stall development has been discussed in detail in previous publications[14,43,44] and is summarized here for reference. From the beginning of the pitch-up motion until the static stall angle is reached at t_{ss}, the flow is attached to the airfoil [Fig. 3(a)]. During this attached flow stage, the spatially averaged shear layer height from instantaneous velocity fields is close to zero and the lift coefficient and positive circulation increase with increasing angle of attack. Beyond the static stall angle α_{ss}, the lift keeps increasing and the flow starts to detach at the trailing edge [Fig. 3(b)]. The trailing edge separation point moves upstream with increasing angle of attack [Figs. 3(b) and 3(c)]. At the interface between the region of flow reversal near the trailing edge and the free stream, a shear layer forms where positive vorticity is concentrated. The vorticity contained in the shear layer is accumulated in small-scale corotating vortices, as a result of a primary shear layer instability or Kelvin-Helmholtz instability.[21,47] The reversed flow region expands with increasing angle of attack, pushing the shear layer further away from the airfoil's suction surface. During this initial spread of the trailing edge separation region, the average shear layer height increases approximately linearly in time and the lift coefficient increases at a lower rate than below the static stall angle (Fig. 4). Later in the cycle, the shear layer vortices start to pair, which initiates the roll-up of the shear layer into a large scale coherent dynamic stall vortex [Figs. 3(c) and 3(d)].[44] The period between the time at which the static stall angle is exceeded and the time at which the shear layer starts to roll up is called the primary instability stage and is highlighted in the figures that present time histories by the light color shading. The period during which the shear layer rolls up into a primary stall vortex is called the vortex formation stage and is highlighted in the figures by the dark color shading.

At the beginning of the shear layer roll-up, the lift coefficient reaches a maximum. During the shear layer roll-up, the lift coefficient decreases while the positive circulation keeps increasing. The average shear layer height now increases at a rate of 15 times higher than during the primary instability stage. Another characteristic

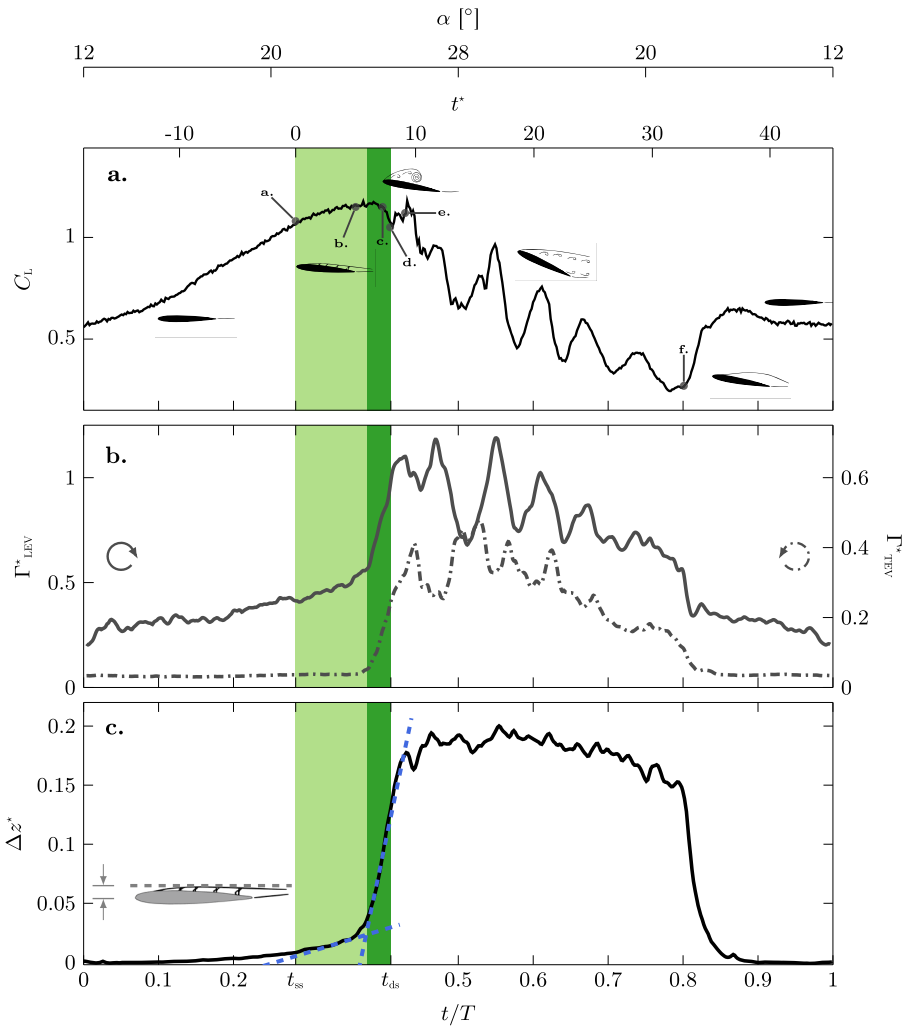

FIG. 4. Temporal evolution of the lift coefficient (a), positive and negative circulation (b), and chord wise average chord-normal shear layer distance (c) during an individual pitching cycle described by $\alpha_0 = 20°$, $\alpha_1 = 8°$, $k = 0.05$, and $\dot{\alpha}^*_{ss} = 0.013$. The labels (a)–(f) in the lift history indicate the timing of the velocity and vorticity field snapshots in Fig. 3. The shaded regions refer to the stall development stages between the time when the static stall angle of attack is exceeded t_{ss} and the dynamic stall onset is reached t_{ds}. The dashed lines in (c) represent the linear fits of Δz^* characteristic for the primary instability and the vortex formation stage.

feature of the second stage of stall development is the emergence of negative vorticity at the airfoil surface underneath the shear layer [Fig. 3(c)]. The induced velocity due to the growing positive circulation of the primary stall vortex pushes the negative vorticity toward the leading edge and ultimately leads to the self-induced detachment of the dynamic stall vortex [Fig. 3(d)].[14,48] The timing of the pinch-off of the dynamic stall vortex is referred to as the dynamic stall onset (t_{ds}). After pinch-off, the dynamic stall vortex is convected downstream and the airfoil is fully stalled [Fig. 3(e)]. During the fully stalled stage of the dynamic stall life cycle, the average shear layer height is maximum and strong fluctuations in the lift coefficient and the circulation are observed which are attributed to the formation and shedding of successive stall vortices.

Near the end of the pitch-down motion, for an angle of attack lower than the static stall angle α_{ss}, the flow reattaches to the airfoil starting from the leading edge [Fig. 3(f)]. During flow reattachment, the lift coefficient increases and the shear layer height and circulation values decrease. At the end of the pitch-down motion, the flow is fully reattached and the lift coefficient has relaxed to the same value obtained at the beginning of the sinusoidal motion.

The time-resolved velocity field data reveal that dynamic stall development is a two-stage process. The first stage, named the primary instability stage, is characterized by an increasing region of flow reversal indicated by a linear growth of the chord normal distance between the shear layer and the airfoil's suction surface. Flow reversal occurs in the boundary layer directly at the airfoil's surface and is not immediately followed by flow separation in a dynamic stall life cycle.[33,49] During this first stage, the lift overshoot with respect to the static stall limit is generated and there is limited interaction between the individual vortices in the shear layer. The second stall development stage, named the vortex formation stage, is characterized by the roll-up of the shear layer into a large coherent dynamic stall vortex. During this second stage, the flow actually separates and the free shear layer no longer follows the airfoil contour. The transition between the primary instability stage and the vortex formation stage was determined directly from the velocity field data as the intersection between the linear fitting curves of the

temporal evolution of the average height of the shear layer [Fig. 4(c)]. The dynamic stall onset was determined by the first peak in the time development coefficient of the proper orthogonal decomposition mode that represents the dynamic stall vortex. The timing of this peak coincides with the departure of the Lagrangian saddle point, which marks the intersection between the attracting and repelling material lines that bound the dynamic stall vortex, away from the surface.[14] The emergence and trajectories of Lagrangian saddle points are not only reliable indicators of the pinch-off or lift-off of coherent leading edge or wake vortices, but they also leave a distinct footprint in the surface pressure distribution and the force history.[50–53]

Time-resolved velocity field data allow for accurate determination of dynamic stall onset, but they cannot be readily utilized as an observable parameter to serve as prediction input for practical applications such as flow control or gust alleviation.[54–58] Inspired by the idea of Niven and Galbraith[33] that an esthetic prediction of dynamic stall onset and the critical leading edge suction should be based on a quantifiable feature of the unsteady trailing edge flow reversal, we aim to derive a theoretical model of the leading edge suction parameter based on the height of the shear layer. Prior to proposing a theoretical model of the leading edge suction parameter based on thin airfoil theory and the evolution of the shear layer height, we will first describe the interplay between the shear layer development and the evolution of the experimentally determined leading edge suction parameter.

IV. LEADING EDGE SUCTION DURING DYNAMIC STALL

A. Leading edge suction parameter

The leading edge suction parameter for our experimental data is derived from the leading edge suction vector $\vec{S}_{\mathrm{LE}}$ which is determined by integrating the pressure signals from the 13 unsteady pressure sensors located in the front 10 % of the airfoil (Fig. 2).[42] Approximately 40% of the lift and 90% of the chord wise force component during the pitch-up motion are generated by the front 10% of the airfoil. Figure 5 presents the phase-averaged evolution of the leading edge suction vector during pitch-up for the example dynamic stall case presented in Fig. 3. The phase-averaged quantities were obtained by averaging over more than 35 pitching cycles. As a measure for the variability of the signals between cycles, we have added the minimum and maximum envelopes. Prior to the dynamic stall vortex pinch-off, the repeatability of the pressure measurements and leading edge suction vector is high and the phase-averaged evolution is representative for all pitching cycles. During the stalled stage, cycle-to-cycle variations of the leading edge suction vector rapidly increase, mainly due to variations in the vortex shedding process and timing.

The leading edge suction vector is characterized by a magnitude S_{LE} [Fig. 5(a)] and an angle λ relative to the inflow velocity direction [Fig. 5(b)]. The experimental leading edge suction parameter A_0 [Fig. 5(c)] is calculated based on the chord wise projection of the leading edge suction vector according to Katz and Plotkin,[39]

$$A_{0,exp} = \sqrt{\frac{2}{\pi}|S_{LE}|\cos(\lambda - \alpha)}. \quad (3)$$

The magnitude of the leading edge suction vector S_{LE} increases during the attached flow and the primary instability stage and decreases during the vortex formation stage. The leading edge suction magnitude reaches a maximum exactly at the transition between the primary instability and the vortex formation stage and a local minimum at the dynamic stall onset. The timing of the stages is determined directly from the velocity field data that do not include information from within the boundary layer, and the leading suction vector only includes information from the front 10% of the airfoil. The concurrence between crucial changes in the flow field and the leading edge suction is remarkable, it confirms the existence of a two-stage stall development, and it is encouraging to further explore the potential of stall criteria based on the leading edge suction.

The orientation of the leading edge suction vector gives us additional information about the location of the region that contributes most to the leading edge suction. During the attached flow and primary instability stage, $\lambda \approx 85°$ and the leading edge suction vector is approximately perpendicular to the incoming flow [Fig. 5(b)]. This indicates that the topology of the flow around the leading edge has not yet been altered during the primary instability stage despite the growing region of flow reversal near the trailing edge. As a consequence, if the pitching direction is reversed prior to the onset of the vortex formation stage, massive flow separation and load hysteresis can be significantly reduced. This condition has been identified in the literature as light dynamic stall.[7,14] During the vortex formation stage, the suction angle slightly decreases first, i.e., suction shifts toward the leading edge, and then increases to $\approx 90°$ at dynamic stall onset. At the beginning of the fully stalled stage, the primary dynamic stall vortex is convected downstream and the leading edge suction vector will roughly point in the direction of the vortex indicated by the rapid increase in the leading edge suction angle up to $\approx 120°$ when the maximum angle of attack is reached.

The leading edge suction vector $\vec{S}_{\mathrm{LE}}$ gives an idea about the spatiotemporal pressure evolution around the leading edge during the different stages of the dynamic stall life cycle and is further condensed in a single leading edge suction parameter that is proposed as a simple but robust parameter that governs leading edge or dynamic stall vortex formation by Ramesh *et al.*[35] The evolution of the leading edge suction parameter is similar to the evolution of the magnitude of the leading edge suction vector with an increase during the attached phase and the primary instability stage, a maximum at the transition between the primary instability and the vortex formation stages, and a decrease during the vortex formation stage [Fig. 5(c)]. The main difference between the evolution of the leading edge suction magnitude and the parameter is the absence of a secondary local suction peak due to the shedding of the primary stall vortex in the suction parameter because the downstream convection of the vortex does not seem to affect the chord wise component of the leading edge suction.

B. Critical values and characteristic time scales

The leading edge suction parameter represents the suction maintained at the leading edge. There is a critical amount of suction that the leading edge can sustain and above which the airfoil stalls.[59] According to Ramesh *et al.*,[38] the critical value of

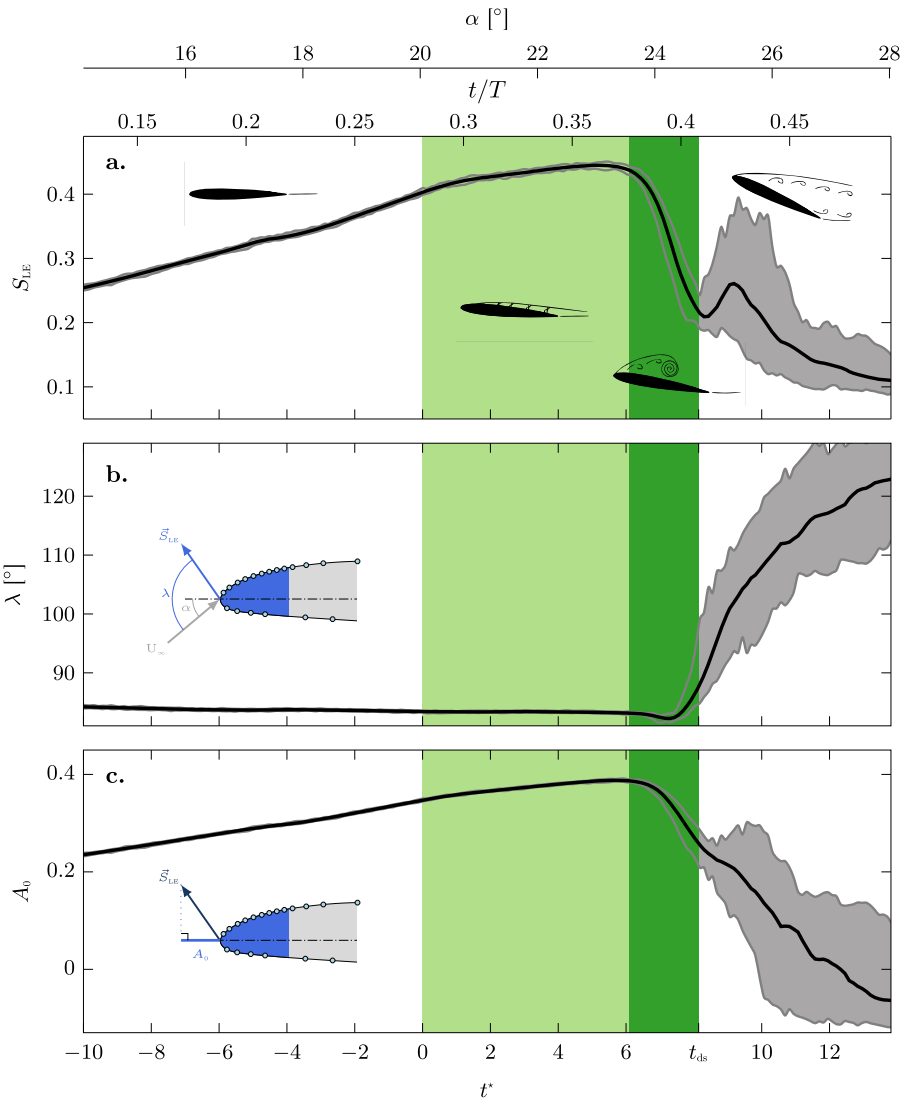

FIG. 5. Magnitude S_{LE} of the leading edge suction force (a), its orientation λ relative to the inflow velocity (b), and the leading edge suction parameter (c) for a pitching motion described by α_0 = 20°, α_1 = 8°, and k = 0.05. The thick black line represents the phase average, and the gray region is delineated by the minimum and maximum envelopes.

the leading edge suction parameter depends mainly on the airfoil shape and the Reynolds number and is independent of the motion kinematics except when high degrees of trailing-edge flow separation occur during the motion. The ideal dynamic stall prediction parameter has a critical value at dynamic stall onset that is largely independent of the flow and motion conditions and can easily be determined or derived for various airfoil geometries. The leading edge suction parameter has strong potential in this direction, but we need to further explore how the temporal evolution of the leading edge suction parameter and its critical values vary with the unsteadiness of the motion kinematics for dynamic stall cases where stall onset is the result of the roll up of the free shear layer bounding the region of flow reversal near the airfoil surface.

The phase-averaged temporal evolution of the experimental leading edge suction parameter for various sinusoidal pitching motions with different amplitudes, mean angles of attack, and pitching frequencies is presented in Fig. 6. The line color indicates the unsteadiness of the harmonic pitching motions in terms of the normalized effective unsteadiness. The latter is defined as the dimensionless pitch rate when the static stall angle of attack is exceeded. It was found to be a suitable scaling parameter for the timing of stall onset by Mulleners and Raffel[14] and Müller-Vahl *et al.*[28] All curves are aligned in time with respect to the time when the static stall angle is exceeded, which is considered the start of the dynamic stall development stage. The lines are solid up to the occurrence of dynamic stall and dashed thereafter.

The general evolution of the leading edge suction parameter is similar for the different motions. It starts with a linear increase during the primary instability stage followed by a linear decrease during the vortex formation stage. For a nonseparated flow, the value of the leading edge suction parameter is related to the angle

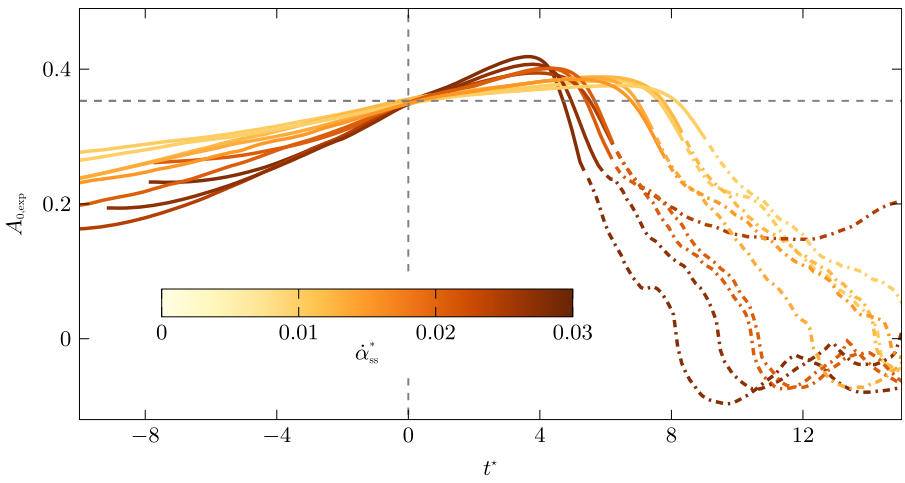

FIG. 6. Temporal evolution of the measured phase-averaged leading edge suction parameter A_0 during the dynamic stall development stage for different normalized effective unsteadiness $\dot{\alpha}^{\star}_{ss}$. The static stall angle is reached at $t^{\star} = 0$. Full lines represent the evolution up to dynamic stall onset, and dashed lines represent the poststall evolution.

of attack and all curves intersect at $t^{\star} = 0$, where the angle of attack equals the static stall angle of attack. During the primary instability stage, the slope of the leading edge suction parameter increases with increasing normalized effective unsteadiness due to the increasing rate of change in the angle of attack around $t^{\star} = 0$. The maximum leading edge suction increases and is reached earlier for higher pitch rates. During the vortex formation stage, which starts sooner for higher normalized effective unsteadiness, the slope increases with increasing unsteadiness. The maximum or critical value of the leading edge suction parameter, which is reached for all motions at the transition between the two stall development stages, is not constant but increases with increasing unsteadiness. This is in line with the recent observations by SureshBabu *et al.*[60]

The characteristic values of the leading edge suction parameter at the start of the stall development stage and the maximum values at the start of the vortex formation stage are summarized in Fig. 7(a) in function of the normalized effective unsteadiness. The maximum value of the leading edge suction parameter increases approximately linearly with increasing unsteadiness, and the same holds for the reciprocal of the convective time at which the maximum value is reached [Fig. 7(b)]. The higher the local pitch rate,

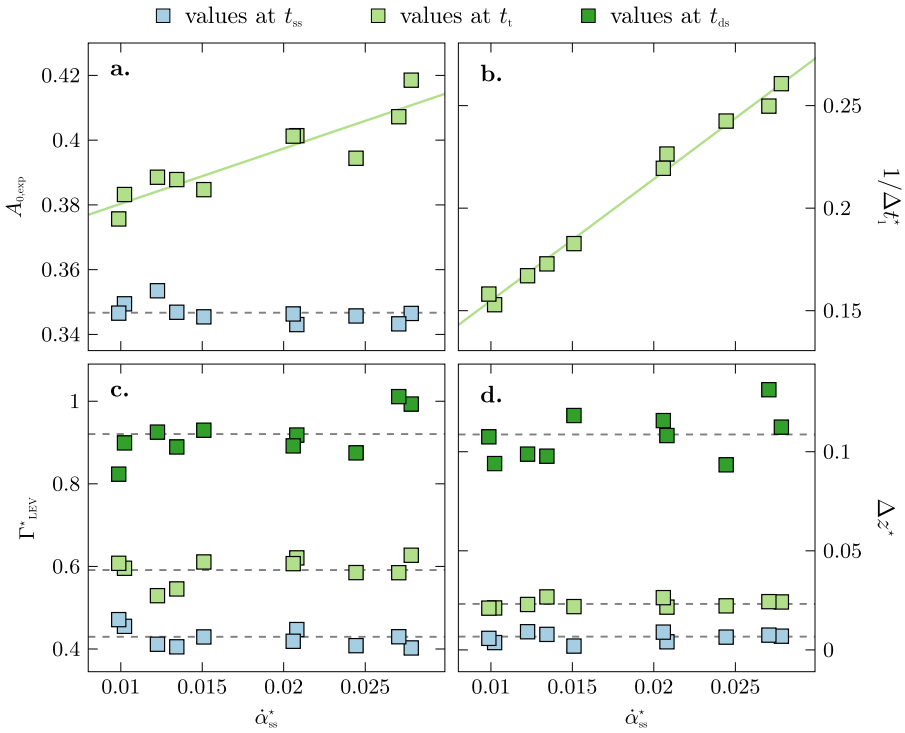

FIG. 7. Characteristic values of the leading edge suction parameter (a), the inverse of the stall delay (b), the positive circulation associated with the leading edge or dynamic stall vortex (c), and the chord wise averaged chord-normal shear layer height (d) in function of the normalized effective unsteadiness. The color of the symbols indicates whether the values represent the situation at the start of the dynamic stall development t_{ss}, at the transition between the two stall development stages t_t, or at dynamic stall onset t_{ds}.

the faster the critical leading edge suction value is reached. At the same time, an increasing lag in the onset of the instability that leads to the roll-up of the shear layer seems to increase the value of the critical amount of suction that is obtained at the leading edge. The deficiency function introduced in Leishman and Beddoes' dynamic stall onset criterion takes into account that a critical value of the leading edge pressure will be reached at a higher value of the normal force coefficient, which in turn will be reached at a higher angle of attack with increasing pitch rate, but it does not consider an increase of the value of the critical leading edge pressure.

The time at which the leading edge suction parameter reaches a maximum coincides with the transition between the two dynamic stall development stages as determined previously based on the evolution of the shear layer height. The durations of the two stall development stages in terms of convective time units are independently quantified based on the global velocity field data and based on the surface pressure data at the leading edge, and results are compared in Fig. 8. We obtain the same resulting time delays for the primary instability stage $\Delta t_1{}^\star$ and the vortex formation stage $\Delta t_2{}^\star$ for both measurements. This result is not trivial. The velocity field measurements do not include information from within the boundary layer near the airfoil's surface. The leading edge suction parameter was calculated taking into account only the surface pressure measurements in the front 10% of the airfoil profile. The fact that we are able to identify two stall development stages in these two independently measured quantities and extract the same associated characteristic time scales for the stall stages clearly demonstrates the direct connection between the evolution of the shear layer height $\Delta z^\star$ and the leading edge suction parameter A_0. This results also underlines the potential of the latter to serve as an observable parameter for the prediction of dynamic stall onset and control applications.

The remaining drawback of the leading edge suction parameter as a universal dynamic stall onset indicator is the variation of its critical value with the unsteadiness of the pitching motion. By linking the leading edge suction to other characteristic parameters that obtain limiting critical values at dynamic stall onset or at the transition between the two stall development stages, we aim to contribute to the applicability and generalizability of a dynamic stall criterion based on the leading edge suction parameter and to a better understanding why dynamic stall happens when it happens.

The durations of the stall development stages reach characteristic values that aid to understand the influence of the motion kinematics on the stall delay. The duration of the vortex formation stage is independent of the normalized effective unsteadiness (Fig. 8). This stage is characterized by the roll-up of the shear layer into a coherent dynamic stall vortex and is predominantly driven by viscous interactions that dependent on the Reynolds number but not on the motion kinematics. This constant time delay corresponds to the empirical time constant that was introduced by Niven and Galbraith[33] as an extension of the Beddoes-Leishman model.

The governing mechanisms during the primary instability stage are different and yield a decreasing time delay with increasing unsteadiness even though the critical leading edge suction increases (Fig. 8). We can also present the reciprocal of the time delay, which decreases linearly with increasing effective unsteadiness [Fig. 7(b)].

Even though the dependence of the stall delay with the motion kinematics is clear, it does not provide a general critical value above which the stall onset is triggered. Motion independent critical values are observed for the shear layer height and positive circulation associated with leading edge vortices [Figs. 7(c) and 7(d)]. For both parameters, the values at the start of dynamic stall development (t_{ss}), at the transition between the two stall development stages (t_t), and at dynamic stall onset (t_{ds}) are constant for all different motions. The values at these key points in the dynamic stall life cycle increase with increasing convective time and progression in the stall development. At dynamic stall onset, the standard deviation of the values from different motions is larger and some minor dependence on the unsteadiness could still be present for the circulation at t_{ds}. As previously concluded, the flow development during the vortex formation stage is governed by viscous interactions and the convective time duration of this stage is independent of the motion kinematics. The relevant critical values for dynamic stall onset are the threshold values at t_t as they trigger the roll-up of the shear layer into the dynamic stall vortex. An increase in circulation within the free shear layer will increase the

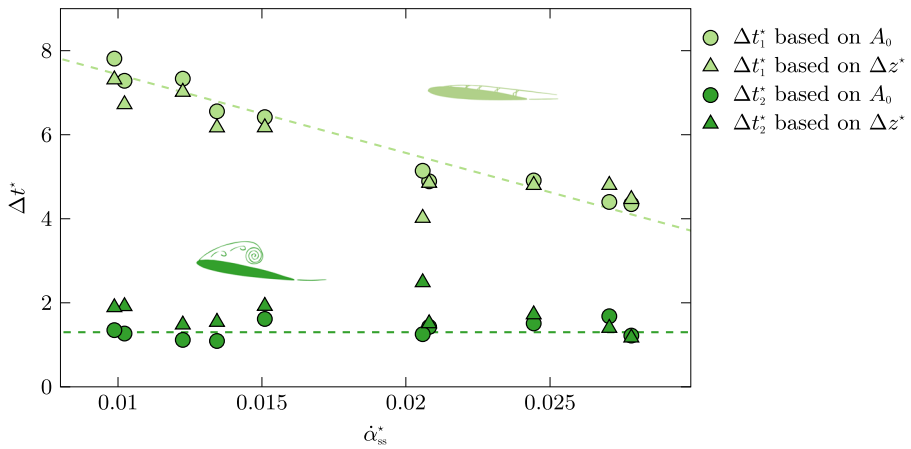

FIG. 8. Time duration of the two stall development stages for different normalized effective unsteadiness measured independently by local pressure measurements (A_0) and by global velocity field measurement ($\Delta z^\star$).

mutual interaction between small scale shear layer vortices[13] and the tendency of the shear layer to roll up. The shear layer can only roll up if its chord normal distance to the airfoil surface is large enough. This explains why both parameters reach critical values at the start of the shear layer roll-up independent of the motion kinematics. The higher the effective unsteadiness of the pitching motion, the sooner the critical circulation threshold is reached and the shorter the stall delay associated with the primary stall development stage.

Critical thresholds of the circulation and the shear layer height are reliable indicators of stall onset for the airfoil profile and Reynolds number considered here. The threshold values are independent of the motion kinematics, but the parameters are not easily accessible outside of the laboratory environment. The leading edge suction parameter is a robust and more practical parameter that could even be determined in flight and serve as an observable for *in situ* flow control applications where early detection of the inception of dynamic stall is essential. Its applicability and reliability hinge upon an *a priori* knowledge of the critical value of the leading edge suction in function of the pitching motion parameters. A low-order model based on thin airfoil theory is proposed in Sec. V to predict the critical values and the evolution of the leading edge suction parameter during dynamic stall development by including the effect of trailing edge flow reversal.

V. THEORETICAL MODEL OF THE LEADING EDGE SUCTION PARAMETER

A. Comparison with thin airfoil theory

The leading edge suction parameter is the first coefficient of the Fourier series of the circulation distribution along the chord. It is calculated by integrating the local induced velocity $v_{\mathrm{ind}}(x,t)$ normal to the surface,

$$A_{0,\mathrm{theor}} = -\frac{1}{\pi}\int_0^{\pi} \frac{v_{\mathrm{ind}}(x,t)}{U_\infty} d\theta. \tag{4}$$

The induced normal velocity represents the deviation of the parallel free stream due to the presence of the airfoil. For a pitching airfoil, the normal induced velocity has three contributions,

$$v_{\mathrm{ind}}(x,t) = -U_\infty \sin\alpha - \dot{\alpha} x_{\mathrm{p}} + \frac{\partial \eta}{\partial x} U_\infty \cos\alpha. \tag{5}$$

The first term represents the effect of the angle of attack; the second term represents the influence of the unsteady pitching motion, where x_{p} is the location of the airfoil's pivot point; and the last term represents the influence of the camber of the airfoil, where $\eta(x)$ is the chord-normal coordinate of the camber line along the chord.

For a sinusoidal pitching motion around the quarter chord, the theoretical leading edge suction parameter reads

$$A_{0,\mathrm{theor}} = \sin\alpha + \dot{\alpha}\frac{c}{4U} - K_\eta \cos\alpha, \tag{6}$$

where

$$K_\eta = \frac{1}{\pi}\int_0^{\pi} \frac{\partial \eta(\theta)}{\partial x} d\theta \tag{7}$$

represents the influence of the airfoil's camber.

The influence of the angle of attack, pitching rate, and camber terms during a pitching motion is presented in Fig. 9 with dashed lines. The theoretical leading edge suction parameter is presented by the dark line, and the experimental phase-averaged leading suction parameter is presented by the bright line. The time on the abscissa is nondimensionalized by the convective time. The time over a pitching period and the angle of attack are indicated on the top. The two stages of the dynamic stall development are marked by the shaded areas.

The first term $\sin\alpha$ is an order of magnitude higher than the other terms. It ranges from 0.2 to 0.4, while the second term composed of the pitch rate is almost zero, and the third term varies around −0.02. The first term is the dominant term in the model of the theoretical leading edge suction parameter and evolves sinusoidally with a maximum for the maximum angle of attack. The

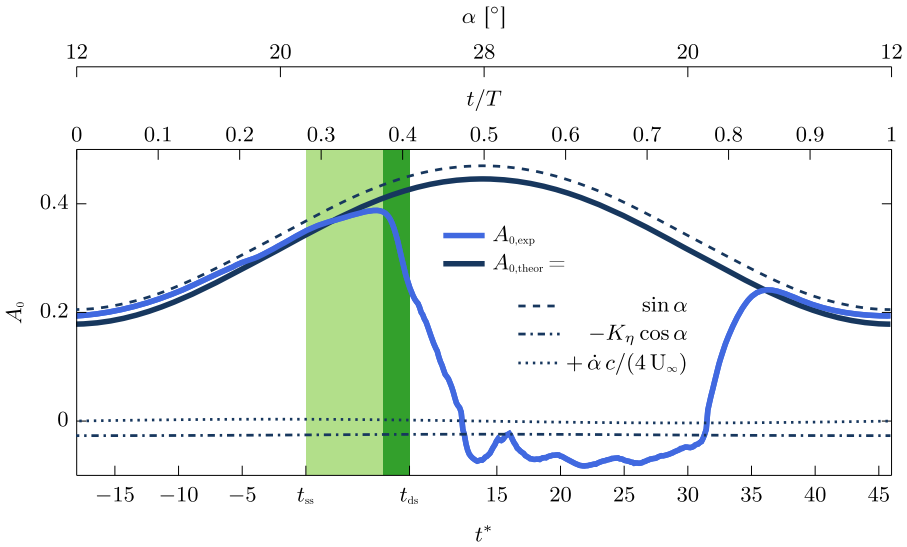

FIG. 9. Comparison of the experimental ($A_{0,\mathrm{exp}}$) and theoretical ($A_{0,\mathrm{theor}}$) leading edge suction parameters for the same motion as presented in Fig. 3. The influence of the different terms in Eq. (6) are presented by the dashed lines.

experimental leading edge suction parameter and its model are in close agreement during the attached flow stage and the reattachment stage.

During the first stage of the dynamic stall development, the experimental leading edge suction parameter $A_{0,\,\mathrm{exp}}$ increases at a slower rate than during the attached flow stage. This is not correctly represented by the theoretical leading edge suction parameter that increases at a higher rate than the experimental leading edge suction parameter. The values of both at the time the static stall angle of attack is reached ($t^\star = 0$) are almost identical. Due to different growth rates during the primary instability stage, the model overestimates the leading edge suction during stall development. At the transition between the primary instability and the vortex formation stage, the experimental leading edge suction parameter reaches a maximum which is not represented by the potential model. During the vortex formation stage, the theoretical leading edge suction parameter continues to increase, while the experimental leading edge suction drops to values close to zero when the flow is separated.

When the flow reversal region spreads from the trailing to the leading edge during the primary instability stage, the curvature of the flow is effectively decreased, reducing the acceleration of the flow around the leading edge and the leading edge suction. This effect is not included in the model presented by Eq. (6). Thin airfoil theory predicts well the increase in the experimental leading edge suction parameter when the flow is attached but needs to be extended to include the growth of the flow reversal region during the primary instability stage.

B. Influence of shear layer on the leading edge suction parameter

The experimental results revealed that the shear layer plays an important role in the dynamic stall development. We propose an improvement of the theoretical model of the leading edge suction parameter by taking into account a twofold influence of the evolution of the shear layer, being a change in the effective camber and a change of the effective angle of attack of the airfoil (Fig. 10).

The position of the shear layer above the airfoil's suction surface virtually increases the thickness of the airfoil. The height of the shear layer is added to the position of the airfoil's suction surface relative to the camber of the airfoil. During the primary instability stage, the shear layer height, which is defined here as the vertical distance between the shear layer and the airfoil's suction surface, is larger near the trailing edge than at the leading edge where the height is almost zero [Fig. 3(b)].

If the height of the shear layer is taken into account, the effective thickness t_{eff} is the sum of the airfoil's geometrical thickness t_{geo} and the shear layer height t_{sl},

$$\forall x,\ t_{\mathrm{eff}}(x) = t_{\mathrm{geo}}(x) + t_{\mathrm{sl}}(x). \tag{8}$$

Using the definition of the purely geometric camber for the airfoil η_{geo},

$$z_{\mathrm{upper,\,geo}} = \eta_{\mathrm{geo}} + \frac{1}{2}t_{\mathrm{geo}}, \tag{9}$$

and the definition of the effective camber for the virtual airfoil profile η_{eff},

$$z_{\mathrm{upper,\,eff}} = \eta_{\mathrm{eff}} + \frac{1}{2}t_{\mathrm{eff}}, \tag{10}$$

we calculate the effective camber of the virtual airfoil profile as a function of the shear layer height and geometric camber,

$$\eta_{\mathrm{eff}} = \eta_{\mathrm{geo}} + \frac{1}{2}t_{\mathrm{sl}}. \tag{11}$$

We now modify the third term of the potential model of the leading edge suction parameter [Eq. (6)] by using the virtually altered airfoil profile according to

$$K_{\eta_{\mathrm{eff}}} = K_\eta + \frac{1}{2\pi}\int_0^\pi \frac{\partial t_{\mathrm{sl}}(\theta)}{\partial x}\,d\theta \tag{12}$$

$$= K_\eta + \Delta z^\star, \tag{13}$$

where $\Delta z^\star$ is the experimentally determined dimensionless chordwise average of the shear layer height.

The first term of this equation (12) represents the influence of the geometric camber according to Eq. (7), and the second term represents the influence of the shear layer height on the effective camber. The growth of the shear layer leads to an increase in effective camber. The chord wise variation of the shear layer height is approximated here by a linear increase from zero at the leading edge to 2 $\Delta z^\star$ at the trailing edge. The linear increase of the shear layer height is a first order approximation that seems reasonable during the primary instability stage [Fig. 3(d)].

The additional consequence of the development of the shear layer is a change in the effective angle of attack. The shear layer has a maximum height at the trailing edge that leads to a change in camber but also an upward shift of the virtual trailing edge and a decrease of the effective angle of attack, which is schematically represented in Fig. 10. The effective angle of attack is given by

$$\alpha_{\mathrm{eff}} = \alpha - \alpha_{\mathrm{sl}}$$
$$= \alpha - \tan\Delta z^\star. \tag{14}$$

This calculation of the effective angle of attack could be further extended to include the effect of varying pivot point locations based on the recent work by Li *et al.*[61]

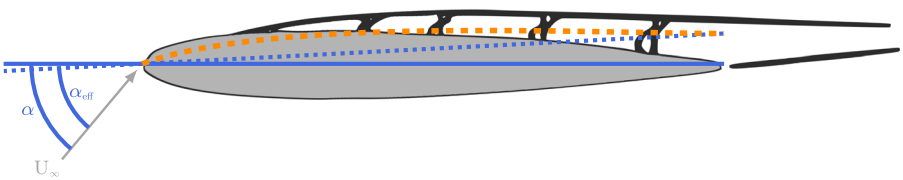

FIG. 10. Schematic representation of the influence of the shear layer growth on the effective angle of attack (α_{eff}) and the effective camber.

The modified model for the leading edge suction parameter taking into account the influence of the shear layer growth during stall development is given by

$$A_{0,\text{theor}'} = \sin\alpha_{\text{eff}} + \dot{\alpha}\frac{c}{4U} - K_\eta \cos\alpha_{\text{eff}} - \Delta z^\star \cos\alpha_{\text{eff}}. \quad (15)$$

By replacing the geometric angle of attack in Eq. (6) by the effective angle of attack and adding a new term, the change in camber due to the presence of the shear layer is taken into account. The first term in Eq. (15) is still an order of magnitude higher than the other terms and is presented in Fig. 11 by the dashed line, along with the newly added term $\Delta z^\star \cos\alpha_{\text{eff}}$ in the dotted-dashed line. Figure 11 also presents the final result of the modified leading edge suction parameter model $A_{0,\text{theor}'}$ by the dark solid line and the experimentally obtained leading edge suction parameter $A_{0,\text{exp}}$ by the bright solid line.

The magnitude of the term $\sin\alpha_{\text{eff}}$ still ranges from 0.2 to 0.4, but its maximum is no longer reached at half period but at the transition between the two stages of the dynamic stall development. When the flow is attached, the geometric and effective angles of attack are close. When the flow starts to separate and when the shear layer rolls up, the shear layer height increases, reducing the effective angle of attack. This leads to a reduction in the contribution of the first term when the flow progressively separates.

The last term $\Delta z^\star \cos\alpha_{\text{eff}}$ in Eq. (15) is negative throughout the cycle and mirrors the evolution of the average shear layer height presented in Fig. 4(c). The term $\Delta z^\star \cos\alpha_{\text{eff}}$ is an order of magnitude lower than the term $\sin\alpha_{\text{eff}}$ (Fig. 11), and the modified theoretical leading edge suction parameter is dominated by the effective angle of attack.

The new model accurately predicts the experimentally obtained leading edge suction parameter during the attached flow, the primary instability stage, and the vortex formation stage. During the primary instability stage, the model correctly predicts the decreasing slope of the experimental leading edge suction. The modified theory predicts a maximum value at the transition between the primary instability and the vortex formation stage and a decrease of the suction at the leading edge during the latter. Both the value and the timing of the maximum leading edge suction are correctly estimated. When the shear layer starts to roll up, the assumptions of the thin airfoil theory reach the boundaries of their validity, but the sharp decrease in the leading edge suction parameter is still correctly modeled. During the fully stalled stage, the modified model of the leading edge suction parameter decreases over time but not sufficiently to match the experimental values. At the end of the pitch down motion, during the reattachment stage, the modified theoretical leading edge suction parameter increases and relaxes at the same rate than the experimental leading edge suction parameter but with a short time lag with respect to the experimental values.

A comparison of the critical values for the experimental and model leading edge suction parameter in function of normalized effective unsteadiness for various motion kinematics is presented in Fig. 12. The experimental values are presented by squares, and the model values taking into account the influence of the shear layer are presented by diamonds. The modified theoretical model predicts well the critical values of the experimental leading edge suction parameter for the range of normalized effective unsteadiness studied.

The general evolution of the modified model of the leading edge suction parameter is dominated by the effective angle of attack. The maximum value of the theoretical leading edge suction parameter is predicted with the correct amplitude at the correct time if the twofold influence of the shear layer is taken into account. The shear layer evolution over the entire airfoil has an influence on the local pressure at the leading edge. The pitch rate has no direct influence on the suction at the leading edge through Eq. (15) for this range of reduced frequencies ($k \in [0.05{:}0.1]$) and at this Reynolds number ($Re = 9.2 \times 10^5$), but it has a strong influence on the flow development on the pitching airfoil and on the shear layer development.[1,8] The influence of the pitch rate on the leading edge suction parameter is thus indirectly taken into account by modeling the effective angle of attack and effective camber variations due to the shear layer development.

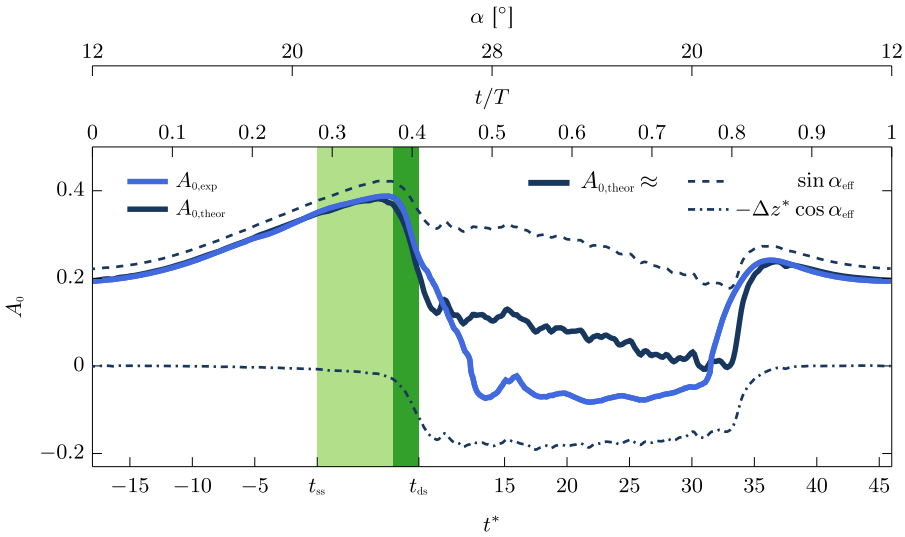

FIG. 11. Comparison of the experimental phase-averaged leading edge suction parameter ($A_{0,\text{exp}}$) and the modified theoretical model ($A_{0,\text{theor}}$) that takes into account the twofold influence of the shear layer on the effective angle of attack and the effective camber. The influence of different terms in Eq. (15) is presented by dashed lines.

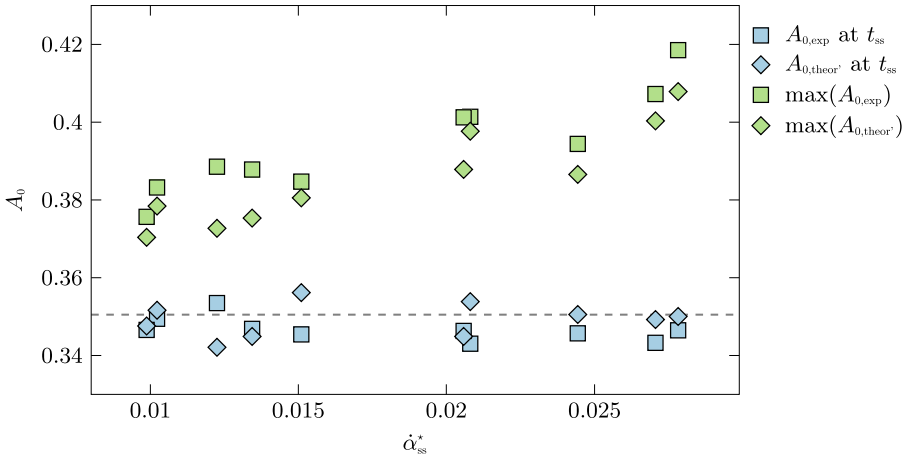

FIG. 12. Values of the leading edge suction parameter, A_0, at t_{ss} when the static stall angle is exceeded, and the maximum values during the dynamic stall development for various motion kinematics in function of the normalized effective unsteadiness.

VI. CONCLUSIONS

The dynamic stall life cycle is analyzed for a sinusoidal pitching motion by time-resolved velocity field and surface pressure measurements. A two-stage dynamic stall development is independently confirmed by the global velocity field measurements and the local airfoil surface pressure measurements around the leading edge. During the first stage, which is called the primary instability stage, the flow separates near the trailing edge and the separation point moves gradually upstream with increasing angle of attack. During this stage, the leading edge suction increases approximately linearly up to a maximum. During the second stage, the vortex formation stage, the shear layer rolls up to create a dynamic stall vortex that pinches off at stall onset. The leading edge suction decreases rapidly during this stage.

The two-stage dynamic stall development is characterized by critical time delays. The time duration of the first stage of the dynamic stall development decreases linearly with increasing motion unsteadiness, promoting an earlier roll-up of the shear layer, while the formation of the dynamic stall vortex and the duration of the vortex formation stage are virtually independent of motion unsteadiness. The critical time delays of the two stages are related to the evolution of the shear layer but are independently extracted from the velocity field measurements above the airfoil and the measurement of the leading edge suction parameter derived from the airfoil surface pressure data around the leading edge.

The leading edge suction parameter condenses the spatiotemporal pressure evolution at the leading edge during the dynamic stall life cycle in one robust parameter. The experimentally obtained values of the leading edge suction parameter are analyzed for various sinusoidal motions. The maximum leading edge suction increases and is reached sooner for increased normalized effective unsteadiness of the pitching motion. During the vortex formation stage, which starts sooner for higher normalized effective unsteadiness, the gradient of the decrease in leading edge suction increases with increasing unsteadiness. The leading edge suction parameter is a practically accessible parameter with high potential to serve as a robust stall onset indicator, but the trigger that leads to the roll-up of the free shear layer is better indicated by motion independent critical values of the chord normal height and the circulation of the shear layer.

An improved model of the leading edge suction parameter is proposed based on thin airfoil theory that links the evolution of the leading edge suction and the shear layer during stall development. The influence of the growth of the shear layer during dynamic stall development on the flow around the airfoil is described in terms of an increase in the effective camber and a decrease in the effective angle of attack of the airfoil. By taking into account this twofold influence of the shear layer development, a new model is derived for the leading edge suction parameter that accurately predicts the value and the timing of the maximum leading edge suction on the pitching airfoil.

ACKNOWLEDGMENTS

The experimental data were acquired at DLR Göttingen in the Department of Helicopters lead by Markus Raffel. We thank Markus for his support during the time of the measurements and for the opportunity to use the experimental data for further analysis. This work was supported by the Swiss National Science Foundation under Grant No. PYAPP2_173652.

REFERENCES

[1]C. Shih, L. Lourenco, L. Van Dommelen, and A. Krothapalli, "Unsteady flow past an airfoil pitching at a constant rate," AIAA J. **30**, 1153–1161 (1992).
[2]A. Spentzos, G. N. Barakos, K. Badcock, B. Richards, P. Wernert, S. J. Schreck, and M. Raffel, "Investigation of three-dimensional dynamic stall using computational fluid dynamics," AIAA J. **43**, 1023–1033 (2005).
[3]W. J. Morris and Z. Rusak, "Stall onset on aerofoils at low to moderately high Reynolds number flows," J. Fluid Mech. **733**, 439–472 (2013).
[4]W. J. McCroskey and R. K. Fisher, "Dynamic stall of airfoils and helicopter rotors," AGARD Report No. 595/5, 1972.
[5]L. W. Carr, K. W. McAlister, and W. J. McCroskey, "Analysis of the development of dynamic stall based on oscillating airfoil experiments," Technical Report No. NASA-TN-D-8382, 1977.
[6]W. J. McCroskey, "The phenomenon of dynamic stall," Technical Report No. 81264, NASA, 1981.
[7]W. J. McCroskey, "Unsteady airfoils," Annu. Rev. Fluid Mech. **14**, 285–311 (1982).

[8]L. W. Carr, "Progress in analysis and prediction of dynamic stall," J. Aircr. **25**, 6–17 (1988).
[9]M. Acharya and H. M. Metwally, "Unsteady pressure field and vorticity production over a pitching airfoil," AIAA J. **30**, 403–411 (1992).
[10]T. Lee and P. Gerontakos, "Investigation of flow over an oscillating airfoil," J. Fluid Mech. **512**, 313–341 (2004).
[11]M. S. H. Boutilier and S. Yarusevych, "Separated shear layer transition over an airfoil at a low Reynolds number," Phys. Fluids **24**, 084105 (2012).
[12]R. Gupta and P. J. Ansell, "Unsteady flow physics of airfoil dynamic stall," AIAA J. **57**, 165–175 (2019).
[13]A. Lambert and S. Yarusevych, "Effect of angle of attack on vortex dynamics in laminar separation bubbles," Phys. Fluids **31**, 064105 (2019).
[14]K. Mulleners and M. Raffel, "The onset of dynamic stall revisited," Exp. Fluids **52**, 779–793 (2012).
[15]M. Bross and D. Rockwell, "Flow structure on a simultaneously pitching and rotating wing," J. Fluid Mech. **756**, 354–383 (2014).
[16]R. Dunne, P. J. Schmid, and B. J. McKeon, "Analysis of flow timescales on a periodically pitching/surging airfoil," AIAA J. **54**, 3421–3433 (2016).
[17]M. Melius, R. B. Cal, and K. Mulleners, "Dynamic stall of an experimental wind turbine blade," Phys. Fluids **28**, 034103 (2016).
[18]E. C. E. Culler and J. A. N. Farnsworth, "Higher frequencies in stall flutter moment development," J. Fluids Struct. **85**, 181–198 (2019).
[19]M. R. Visbal and D. J. Garmann, "Analysis of dynamic stall on a pitching airfoil using high-fidelity large-eddy simulations," AIAA J. **56**, 46–63 (2018).
[20]S. I. Benton and M. R. Visbal, "The onset of dynamic stall at a high, transitional Reynolds number," J. Fluid Mech. **861**, 860–885 (2019).
[21]M. E. Rosti, M. Omidyeganeh, and A. Pinelli, "Direct numerical simulation of the flow around an aerofoil in ramp-up motion," Phys. Fluids **28**, 025106 (2016).
[22]R. Jain, A. Le Pape, A. Grubb, M. Costes, F. Richez, and M. Smith, "High-resolution computational fluid dynamics predictions for the static and dynamic stall of a finite-span OA209 wing," J. Fluids Struct. **78**, 126–145 (2018).
[23]A. T. Degani, Q. Li, and J. D. A. Walker, "Unsteady separation from the leading edge of a thin airfoil," Phys. Fluids **8**, 704–714 (1996).
[24]B. J. Pruski and R. D. W. Bowersox, "Leading-edge flow structure of a dynamically pitching NACA 0012 airfoil," AIAA J. **51**, 1042–1053 (2013).
[25]A. Widmann and C. Tropea, "Parameters influencing vortex growth and detachment on unsteady aerodynamic profiles," J. Fluid Mech. **773**, 432–459 (2015).
[26]S. I. Benton and M. R. Visbal, "Effects of leading-edge geometry on the onset of dynamic stall," AIAA J. **56**, 4195–4198 (2018).
[27]A. Choudhry, R. Leknys, M. Arjomandi, and R. Kelso, "An insight into the dynamic stall lift characteristics," Exp. Therm. Fluid Sci. **58**, 188–208 (2014).
[28]H. F. Müller-Vahl, G. Pechlivanoglou, C. N. Nayeri, C. O. Paschereit, and D. Greenblatt, "Matched pitch rate extensions to dynamic stall on rotor blades," Renewable Energy **105**, 505–519 (2017).
[29]C. Bose and S. Sarkar, "Investigating chaotic wake dynamics past a flapping airfoil and the role of vortex interactions behind the chaotic transition," Phys. Fluids **30**, 047101 (2018).
[30]W. T. Evans and K. W. Mort, "Analysis of computed flow parameters for a set of sudden stalls in low-speed two-dimensional flow," Technical Note D-85, NASA, 1959.
[31]J. G. Leishman and T. S. Beddoes, "A semi-empirical model for dynamic stall," J. Am. Helicopter Soc. **34**, 3–17 (1989).
[32]L. C. Woods, *The Theory of Subsonic Plane Flow* (Cambridge University Press, 1961).
[33]A. J. Niven and R. A. M. Galbraith, "Modelling dynamic stall vortex inception at low Mach numbers," Aeronaut. J. **101**, 67–76 (1997).
[34]W. Sheng, R. A. M. Galbraith, and F. N. Coton, "A new stall-onset criterion for low speed dynamic-stall," J. Sol. Energy Eng. **128**, 461–471 (2005).
[35]K. Ramesh, A. Gopalarathnam, K. Granlund, M. V. Ol, and J. R. Edwards, "Discrete-vortex method with novel shedding criterion for unsteady aerofoil flows with intermittent leading-edge vortex shedding," J. Fluid Mech. **751**, 500–538 (2014).
[36]S. Narsipur, A. Gopalarathnam, and J. R. Edwards, "Low-order model for prediction of trailing-edge separation in unsteady flow," AIAA J. **57**, 191–207 (2019).
[37]D. Darakananda and J. D. Eldredge, "A versatile taxonomy of low-dimensional vortex models for unsteady aerodynamics," J. Fluid Mech. **858**, 917–948 (2019).
[38]K. Ramesh, K. Granlund, M. V. Ol, A. Gopalarathnam, and J. R. Edwards, "Leading-edge flow criticality as a governing factor in leading-edge vortex initiation in unsteady airfoil flows," Theor. Comput. Fluid Dyn. **32**, 109–136 (2018).
[39]J. Katz and A. Plotkin, *Low-Speed Aerodynamics*, Cambridge Aerospace Series, 2nd ed. (Cambridge University Press, 2004).
[40]I. E. Garrick, "Propulsion of a flapping and oscillating airfoil," Technical Report No. NACA-TR-567, National Advisory Committee for Aeronautics; Langley Aeronautical Laboratory, Langley Field, VA, USA, 1936.
[41]P. G. Wilby, "The aerodynamic characteristics of some new RAE blade sections, and their potential influence on rotor performance," Vertica **4**, 121–133 (1980).
[42]J. Deparday and K. Mulleners, "Critical evolution of leading edge suction during dynamic stall," J. Phys.: Conf. Ser. **1037**, 022017 (2018).
[43]K. Mulleners and M. Raffel, "Dynamic stall development," Exp. Fluids **54**, 1469–1477 (2013).
[44]P. Ansell and K. Mulleners, "Multiscale vortex characteristics of dynamic stall from empirical mode decomposition," AIAA J. (published online).
[45]D. Garcia, "A fast all-in-one method for automated post-processing of PIV data," Exp. Fluids **50**, 1247–1259 (2010).
[46]L. Graftieaux, M. Michard, and N. Grosjean, "Combining PIV, POD and vortex identification algorithms for the study of unsteady turbulent swirling flows," Meas. Sci. Technol. **12**, 1422–1429 (2001).
[47]C.-M. Ho and P. Huerre, "Perturbed free shear layers," Annu. Rev. Fluid Mech. **16**, 365–424 (1984).
[48]V. J. Peridier, F. T. Smith, and J. D. A. Walker, "Vortex-induced boundary-layer separation. Part 2. Unsteady interacting boundary-layer theory," J. Fluid Mech. **232**, 133–165 (1991).
[49]W. McCroskey, L. Carr, and K. McAlister, "Dynamic stall experiments on oscillating airfoils," AIAA J. **14**, 57–63 (1976).
[50]D. E. Rival, J. Kriegseis, P. Schaub, A. Widmann, and C. Tropea, "Characteristic length scales for vortex detachment on plunging profiles with varying leading-edge geometry," Exp. Fluids **55**, 1660 (2014).
[51]Y. Huang and M. A. Green, "Detection and tracking of vortex phenomena using Lagrangian coherent structures," Exp. Fluids **56**, 147–158 (2015).
[52]M. P. Rockwood, K. Taira, and M. A. Green, "Detecting vortex formation and shedding in cylinder wakes using Lagrangian coherent structures," AIAA J. **55**, 15–23 (2017).
[53]S. Krishna, M. A. Green, and K. Mulleners, "Flowfield and force evolution for a symmetric hovering flat-plate wing," AIAA J. **56**, 1360–1371 (2018).
[54]S. L. Brunton, S. T. M. Dawson, and C. W. Rowley, "State-space model identification and feedback control of unsteady aerodynamic forces," J. Fluids Struct. **50**, 253–270 (2014).
[55]C. W. Rowley and S. T. Dawson, "Model reduction for flow analysis and control," Annu. Rev. Fluid Mech. **49**, 387–417 (2017).
[56]D. Bhattacharjee, M. Hemati, B. Klose, and G. Jacobs, "Optimal actuator selection for airfoil separation control," in *2018 Flow Control Conference* (American Institute of Aeronautics and Astronautics, Atlanta, Georgia, 2018).
[57]J.-C. Loiseau, B. R. Noack, and S. L. Brunton, "Sparse reduced-order modelling: Sensor-based dynamics to full-state estimation," J. Fluid Mech. **844**, 459–490 (2018).
[58]J. Kou and W. Zhang, "Dynamic mode decomposition with exogenous input for data-driven modeling of unsteady flows," Phys. Fluids **31**, 057106 (2019).
[59]J. Katz, "A discrete vortex method for the non-steady separated flow over an airfoil," J. Fluid Mech. **102**, 315–328 (1981).
[60]A. SureshBabu, K. Ramesh, and A. Gopalarathnam, "Model reduction in discrete-vortex methods for unsteady airfoil flows," AIAA J. **57**, 1409–1422 (2019).
[61]X. Li, L.-H. Feng, and Z.-Y. Li, "Flow mechanism for the effect of pivot point on the aerodynamic characteristics of a pitching airfoil and its manipulation," Phys. Fluids **31**, 087108 (2019).